



ISTITUTO NAZIONALE DI RICERCA METROLOGICA Repository Istituzionale

Correlating the properties of near-room-temperature first- and second-order magnetocaloric materials

This is the author's submitted version of the contribution published as:

Original

Correlating the properties of near-room-temperature first- and second-order magnetocaloric materials / Corrêa, Lorenzo S.; Vieira, Bernardo P.; Lozano, Jaime A.; Barbosa, Jader R.; Rowe, Andrew; Kuepferling, Michaela; Basso, Vittorio; Trevizoli, Paulo V.. - In: JOURNAL OF MAGNETISM AND MAGNETIC MATERIALS. - ISSN 0304-8853. - 566:(2023), p. 170292. [10.1016/j.jmmm.2022.170292]

Availability:

This version is available at: 11696/76220 since: 2023-03-01T09:11:22Z

Publisher:

Elsevier

Published

DOI:10.1016/j.jmmm.2022.170292

Terms of use:

This article is made available under terms and conditions as specified in the corresponding bibliographic description in the repository

Publisher copyright

(Article begins on next page)

Correlating the Properties of Near-Room-Temperature First- and Second-Order Magnetocaloric Materials

Lorenzo S. Corrêa,¹ Bernardo P. Vieira,² Jaime A. Lozano,² Jader R. Barbosa Jr.,²
Andrew Rowe,³ Michaela Kuepferling,⁴ Vittorio Basso,⁴ and Paulo V. Trevizoli^{1, a)}

¹⁾*Department of Mechanical Engineering, Federal University
of Minas Gerais (UFMG), Belo Horizonte - MG, 31270-901,
Brazil.*

²⁾*Department of Mechanical Engineering, Federal University of Santa Catarina,
Florianopolis - SC, 88040-900, Brazil.*

³⁾*Institute for Integrated Energy Systems (IESVIC), University of Victoria,
Victoria - BC, V8W2Y2, Canada.*

⁴⁾*Istituto Nazionale di Ricerca Metrologica, Strada delle Cacce 91, 10135 Torino,
Italy.*

(Dated: 21 July 2022)

Several magnetocaloric materials have been proposed since the discovery of the Giant Magnetocaloric Effect. Although some have great potential as magnetocaloric refrigerants or working materials in thermomagnetic motors/generators, only a few have been tested experimentally or had their properties incorporated into validated mathematical models. While experiments are limited by material costs and specialized equipment to determine magnetic field-dependent properties such as specific heat capacity and magnetization, the development of correlation methods must ensure data quality and resolution over a wide range of conditions to reduce interpolations errors. Aiming to keep the number of baseline experimental data points at a minimum, we propose a fitting procedure to correlate thermomagnetic quantities (i.e., isofield specific heat capacity, magnetization and isothermal entropy change) that is accurate at intermediate (i.e., not directly measured) temperatures and applied magnetic fields. The method has been applied to different first-order materials ($\text{La(Fe,Mn,Si)}_{13}\text{H}_y$ and $\text{MnFeP}_x\text{As}_{1-x}$) and second-order materials (Gd and $\text{Gd}_{100-x}\text{Y}_x$) with a good reproducibility of the isofield specific heat capacity, entropy-temperature diagram, adiabatic temperature change and magnetization behavior around room temperature at applied fields between 0 and 2 T.

^{a)}Electronic mail: trevizoli@demec.ufmg.br

I. INTRODUCTION

Thermomagnetic conversion systems, such as active magnetic regenerators (AMR)^{1,2} and thermomagnetic motors/generators (TMM/TMG)^{3,4}, are promising alternative technologies for cooling and energy harvesting, respectively. In the past twenty years, several experimental apparatuses^{4,5} and validated numerical models^{6,7} have been developed. Most of these works used gadolinium (Gd) as the magnetocaloric material due to its commercial availability in several geometries (plates, spheres, pins) and well-known thermal and magnetic properties.

Current developments in this field are motivated by prospectively more efficient magnetocaloric devices based on first-order (FOM) or second-order transition materials (SOM) with better properties than Gd^{8–11}. In magnetic cooling, the material can be arranged as a multilayer AMR^{12–15} to produce greater temperature spans, larger cooling capacities and higher coefficients of performance (COP). For TMM/TMG, FOMs with high specific magnetization associated with an abrupt variation around the transition temperature may enhance the magnetic force and the produced power.

However, testing and implementing novel materials in lab scale devices and prototypes is not an easy task. Experimental works are limited by high material costs and accessibility to a wide range of compositions, which is also a limiting factor regarding the development of robust correlations and equations of state. Moreover, for most FOM and SOM, the specific heat capacity, magnetization, isothermal entropy change (ΔS_T) and adiabatic temperature change (ΔT_{ad}) data are restricted to applied magnetic fields above 2 T^{16–18}, which is higher than the fields state-of-the-art AMR permanent magnet circuits are usually able reach^{1,19}. Although a few works presented properties at lower applied fields, the resolution regarding intermediate values was still low, sometimes limited to 0.5-T intervals over the 0-1.5 T range^{20–22}.

The lack of data at intermediate fields is exacerbated by the non-linearity of the field-dependent properties (e.g., specific heat capacity, magnetization), giving rise to significant interpolation errors that are propagated along successive numerical iterations leading to convergence issues or spurious results. Hence, combining high-resolution experimental databases (for temperature and magnetic field) with physically-based models^{23–26} (or semi-empirical interpolation schemes that capture the magnetic field dependence) is the most logical ap-

proach to generating computationally efficient models.

Risser *et al.*²⁷ proposed a method to obtain magnetocaloric effect data as a function of the internal magnetic field for SOM. The method is based on some initial experimental data and, through thermodynamic equations and shape functions, the outputs are high-resolution specific heat capacity, magnetization, Δs_T and ΔT_{ad} data. The method was tested only with Gd at fields ranging from 0 to 2 T in steps of 0.05 T, showing good reproducibility and accuracy.

The research group at the University of Victoria developed a *synthetic model* based on Lorentzian curves with empirical constants to fit the specific heat capacity and the entropy of FOM as a function of temperature and magnetic field. Although the model was cited in some works^{28,29}, it remains largely unpublished; its capability to predict properties at intermediate fields (i.e., not directly measured) has not been reported.

Hess *et al.*³⁰ proposed a phenomenological model based on a Cauchy-Lorentz function to correlate the specific heat capacity data of a first-order La(Fe,Mn,Si)₁₃-based alloy as a function of temperature and magnetic field. All relevant properties, i.e., the entropy curves, Δs_T and ΔT_{ad} , are derived from the correlation, making the model thermodynamically consistent. Although the model reproduced the La(Fe,Mn,Si)₁₃-based alloy data satisfactorily, no results were presented for intermediate fields.

Maiorino *et al.*³¹ used Artificial Neural Networks to compute the specific heat capacity, Δs_T and ΔT_{ad} of first-order La(Fe,Co,Si)-based alloys. The calculation procedure was incorporated into a numerical model to simulate multilayer AMRs, improving its accuracy compared to the Curie temperature-shift method.

Paixão *et al.*³² proposed a set of thermodynamic equations to calculate intermediate-field (higher than 0) specific heat capacity and entropy curves for any caloric (i.e., magneto, electro, elasto or barocaloric) material. These properties are the most complex to be experimentally characterized. The input data are the zero-field specific heat capacity and ΔT_{ad} at any applied field, which require less sophisticated equipment and methods. However, the method only works at finite-field data if the experimental ΔT_{ad} is available.

The present work advances a mathematical procedure to compute the thermomagnetic properties of FOM and SOM, having as input specific heat capacity data at discrete values of temperature and applied magnetic fields (baseline data). Fitting expressions are proposed for the specific heat capacity at intermediate temperatures and magnetic fields.

Based on thermodynamic relationships, fitting expressions are also proposed for entropy and magnetization as a function of temperature and applied magnetic field ranges within the baseline data envelope. Relevant magnetocaloric properties, Δs_T and ΔT_{ad} , are derived from the entropy expressions. The model was tested against data for $\text{La(Fe,Mn,Si)}_{13}\text{H}_y$ (FOM), $\text{MnFeP}_x\text{As}_{1-x}$ (FOM with hysteresis) and Gd alloys (SOM). The results accurately reproduced the baseline data and correlated the properties at intermediate fields with remarkable consistency. The routine is available as an open-source code to be tested and improved by the magnetocalorics community.

II. MATHEMATICAL MODEL

A. Algorithm Structure

Figure 1 presents the algorithm to develop the correlations for the specific heat capacity, $T-s$ diagram, isothermal entropy change, adiabatic temperature change and magnetization as a function of temperature and magnetic field. Note that the *intermediate fields* are the applied magnetic field intensities between the values provided as baseline experimental data.

The algorithm is divided into ten steps. The input data consists of experimental (baseline) data on the isofield specific heat capacity, initial (or reference) entropy and magnetization as a function of temperature and magnetic field. In Fig. 1, the blocks/text in black are the algorithm calculations, while those in blue are (optional) verification steps. The parts in red are the points where the temperature and magnetic field ranges and increments (resolution) can be modified.

The algorithm was implemented as an open-source code in Python using the cross-platform integrated development environment Spyder. The FOM and SOM versions of the code are available online at: https://github.com/lorenzosc/material_properties.

Each step of the algorithm is explained in detail in the sections below. For a better understanding of the methods, the reader will be directed, at each step, to the results for $\text{La(Fe,Mn,Si)}_{13}\text{H}_y$ presented in Section III A.

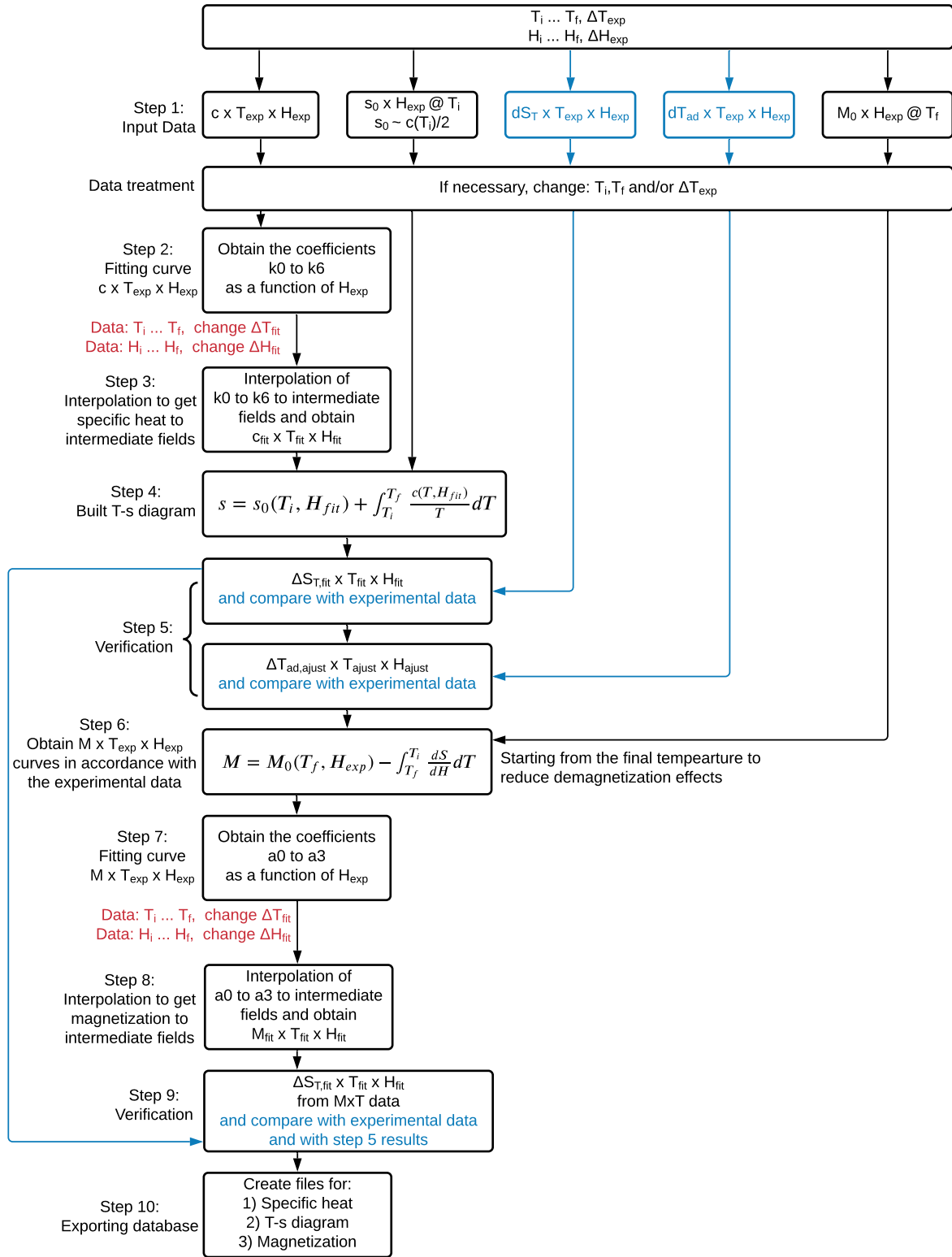


FIG. 1. Structure of the data fitting algorithm for magnetocaloric properties.

B. Input Experimental Data

The algorithm initially receives the temperature and applied magnetic field ranges (T_{exp} and H_{exp}) of the baseline experimental data. The subscripts ‘i’ and ‘f’ denote the initial (lowest) and final (highest) values of the range (see Fig. 1). The temperature and field increments are also received, with the following recommendations:

- At least four magnetic fields with fixed increments are preferred (e.g., 0, 0.5, 1.0, and 1.5 T). However, the code can be easily adapted if non-uniform increments are available. Some databases with three magnetic field values and non-uniform increments were tested (e.g., 0, 1.0 and 1.5 T), and the algorithm may work well after some modifications, although it is more susceptible to interpolation errors;
- The temperature data need to cover values well below and above the magnetic transition temperature (T_{trans}), as this helps to improve the overall precision of the interpolation. In some cases, some data points at the ends of the interval may need to be discarded to improve accuracy. Although no limitation on the temperature increment was noted, the use of uniform increments is encouraged. Also, the region surrounding T_{trans} must be precisely characterized.

As can be seen from Fig. 1, Step 1 reads five different files from experimental measurements: (A) isofield specific heat capacity (c) as a function of T_{exp} and H_{exp} ; (B) reference (initial) entropy value (s_0) as a function of H_{exp} at the initial temperature (T_i); (C) isothermal entropy change as a function of T_{exp} and H_{exp} ; (D) adiabatic temperature change as a function of T_{exp} and H_{exp} ; (E) reference (final) magnetization value (M_0) for all H_{exp} at the final temperature (T_f). It should be noted that:

- The isofield specific heat data are the main input. In (A), if no intermediate field specific heat data are available, the method of³² can be used. The baseline isobaric specific heat data for $\text{La}(\text{Fe,Mn,Si})_{13}\text{H}_y$ are presented in Section III A, Fig. 4(a) (open symbols);
- In (B), s_0 is a reference value for the initial entropy to build the $T - s$ diagram. In the absence of experimental data, it can be approximated by $s_0(T_i, 0) \approx c(T_i, 0)/2$ and $s_0(T_i, H) \approx c(T_i, 0)/2 + \Delta s_0(T_i, \Delta H)$ ^{33,34},

- The (C) and (D) data help verify the fitting procedure against the experimental results. Although such a comparison is not mandatory, it is recommended as a consistency check;
- In (E), M_0 is used to built the magnetization curves. As will be explained later, M_0 is evaluated at T_f to reduce the influence of demagnetizing field losses on the predicted magnetization curves.

For some input data, especially the specific heat capacity, the temperature range may be too extensive or measured with a high resolution (small temperature increments), giving rise to noise in the experimental data. Thus, data treatment may be necessary to remove some points or cut out temperature intervals to reduce this effect. This data treatment is illustrated in the algorithm before Step 2 (see Fig. 1) and it is already implemented in the code. The user is directly guided to set the cut-out ranges and/or change the data resolution, with no need to rebuild the input data file.

C. Specific Heat Capacity Fitting Equation and Interpolation for Intermediate Fields

In Step 2, a mathematical expression is proposed to fit the $c(T, H) \times T$ data with field-dependent coefficients. For FOM, the Pearson type IV asymmetric distribution^{35,36} is used:

$$c_{\text{fit}}(T, H) = k_0(H) + k_1(H) \frac{\left[1 + \left(\frac{T - k_6(H) - k_2(H)}{k_3(H)}\right)^2\right]^{-k_4(H)}}{\left[1 + \left(\frac{k_5(H)^2}{4k_4(H)^2}\right)^{-k_4(H)}\right]} \times \exp \left[-k_5(H) \arctan \left(\frac{T - k_6(H) - k_2(H)}{k_3(H)} \right) + \arctan \left(\frac{k_5(H)}{2k_4(H)} \right) \right] \quad (1)$$

where $k_0(H)$ to $k_6(H)$ are the field-dependent fitting coefficients. In Section III A, Fig. 4(a) illustrates the fitted curves (solid lines) and the experimental data for $\text{La}(\text{Fe}, \text{Mn}, \text{Si})_{13}\text{H}_y$.

Next, in Step 3, interpolations are carried out to determine the values of $k_0(H)$ to $k_6(H)$ at intermediates fields. Linear, quadratic or cubic fits can be tested for better accuracy. Notice, however, that before Step 3 (see Fig. 1), one must specify the temperature and magnetic field increments (ΔT_{fit} and ΔH_{fit}) to generate the specific heat capacity curves

at intermediate fields. Then, the new set of interpolated field-dependent constants are re-inserted into Eq. 1 to calculate the specific heat capacity curves at intermediate fields, as illustrated in Fig. 2(a). In Section III A, Fig. 4(b) exhibits these curves for $\text{La}(\text{Fe,Mn,Si})_{13}\text{H}_y$.

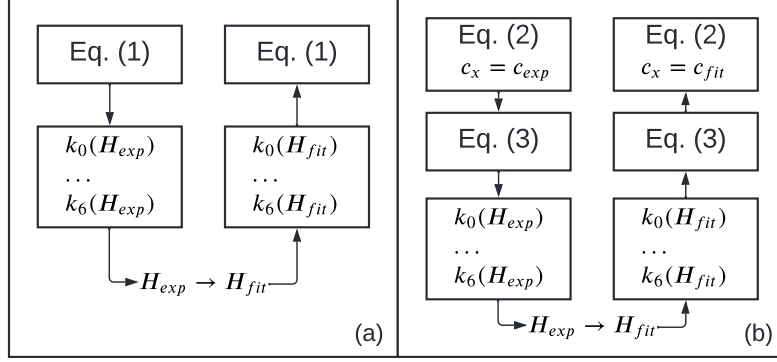


FIG. 2. Steps 2 and 3 of the data fitting algorithm. Calculation of the specific heat capacity at intermediate fields: (a) FOM; (b) SOM.

For SOM, the zero-field specific heat capacity is discontinuous around T_{trans} , whereas the intermediate-field curves are continuous and differ from the one at zero-field. As a result, a single fitting expression can be employed for the intermediate-field data but not for 0 T, for which a different approach is used.

Again, at least four baseline specific heat capacity curves are required (recommended), and, if possible, one of the intermediate-field values should be as close as possible to 0 T (≤ 0.5 T). For instance, for SOM, considering 0, 0.5, 1 and 1.5-T baseline fields, the following fitting expressions are proposed for the intermediate-field $c(T, H) \times T$ data (0.5 to 1.5 T):

$$c^t(T, H) = \left(\frac{c_x(T, H)}{c_{\text{peak}}} \right)^2 (T_f - T + \delta) \quad (2)$$

$$c_{\text{fit}}^t(T, H) = \frac{k_0(H) + k_2(H)T^{0.5} + k_4(H)T + k_6(H)T^{1.5}}{1 + k_1(H)T^{0.5} + k_3(H)T + k_5(H)T^{1.5}} \quad (3)$$

where c_x is an experimental or fitted specific heat capacity, c_{peak} is the maximum specific heat capacity among all the (baseline) experimental magnetic fields (it is treated as a constant in the analysis and, probably, corresponds to the peak value at 0 T) and δ is a constant arbitrarily taken as $\delta = 20$ K. For SOM, no equation was sufficiently accurate to be applied directly to the experimental data. Thus, it was first necessary to perform a variable transformation (converting $c_x = c_{\text{exp}}$ into c^t) using Eq. 2. Then, Eq. 3 is applied to c^t to find the

field-dependent fitting coefficients $k_0(H)$ to $k_6(H)$. The variable transformation is proposed to simplify the data (c^t has a close to linear dependence with temperature), making possible to employ a simpler fitting expression (Eq. 3).

For SOM, Step 3 also has some particularities:

- As the specific heat capacity behaves differently at low fields (0 to 0.5 T). An interpolation involving all the experimental data is employed to predict the specific heat at intermediate fields within this range. To avoid affecting the quality of the results at low fields, intermediate-field data as close as possible to 0 T are necessary.
- For the higher fields (≥ 0.5 T), a similar approach adopted for FOM determines the interpolated field-dependent constants. The new set of coefficients $k_0(H)$ to $k_6(H)$ is inserted in Eq. 3 to calculate the transformed c^t variable. After that, Eq. 2 calculates the intermediate field specific heat capacity making $c_x = c_{\text{fit}}$, see Fig. 2(b).

Notice that, since Eq. 3 is a polynomial fit, oscillations may occur at the edges of the interval. Although one can reduce the fluctuations by adjusting the value of δ , the edges should be removed if the oscillations persist. The edges removal procedure is already implemented in the code, and hence, the data output is made available in accordance with the user-defined temperature range.

D. T-s Diagram and the Magnetocaloric Effect

After obtaining the intermediate field specific heat capacity data, the temperature-entropy ($T - s$) diagram can be built. In Step 4, the entropy curves are determined by^{8,25,33,37}:

$$s(T, H) = s_0(T_i, H) + \int_{T_i}^{T_f} \frac{c(T, H)}{T} dT \quad (4)$$

where s_0 is the previously mentioned reference entropy evaluated at the initial temperature. Figure 5 presents the $T - s$ diagram for $\text{La}(\text{Fe,Mn,Si})_{13}\text{H}_y$. The isothermal entropy change, ΔS_T , and the adiabatic temperature change, ΔT_{ad} , can be determined as a function of T and H as follows:

$$\Delta S_T = s(T, H_f) - s(T, H_i) \quad (5)$$

$$s(T_i + \Delta T_{\text{ad}}, H_f) = s(T_i, H_i) \quad (6)$$

A comparison of the above quantities with experimental data for $\text{La}(\text{Fe,Mn,Si})_{13}\text{H}_y$ FOM is presented in Fig. 6(a) and (c), respectively.

E. Magnetization Fitting and Interpolation for Intermediate Fields

The isothermal entropy change, ΔS_T , can be calculated indirectly from specific heat capacity or magnetization data^{33,38}. Also, when the ΔS_T and ΔT_{ad} data are obtained experimentally from specific heat capacity measurements, experimental magnetization data are generally not available. Here, a procedure is proposed to generate magnetization curves ($M(T, H) \times T \times H$) from the entropy data. In Step 6, the following relation is used³⁷:

$$M(T, H) = M_0(T_f, H) - \int_{T_f}^{T_i} \frac{\partial s(T, H)}{\partial H} dT \quad (7)$$

where the reference magnetization, M_0 , is obtained from experimental data or adjusted from a similar material. Notice that the field-dependent M_0 is evaluated at T_f . Moreover, since a paramagnetic phase exists at the highest temperatures, the $M(T, H) \times T$ curves for a fixed H are built from the highest to the lowest temperature to reduce demagnetization losses^{27,39–41}. Therefore, to perform Steps 6 to 9, one needs to know M_0 (or have it characterized) at different applied fields at the highest temperatures.

From Steps 6 to 8, the procedure is analogous to that for the specific heat capacity. First, to reduce errors, Eq. 7 is applied only to the entropy curves obtained from the experimental (baseline) specific heat capacity data (and not to all intermediate fields in the $T - s$ diagram), to produce a set of magnetization curves called M_{calc} . For the sake of the fitting procedure, the resulting $M \times T$ curves are considered the baseline magnetization data for the experimental temperature and magnetic fields, i.e., $M_{\text{calc}}(T_{\text{exp}}, H_{\text{exp}})$. Figure 7(a) presents the M_{calc} results for $\text{La}(\text{Fe,Mn,Si})_{13}\text{H}_y$ obtained from Eq. 7. Note that if experimental magnetization data are available, the above calculation procedure based on Eq. 7 is not necessary, and the data are the input for the next step.

Step 7 consists of fitting the $M_{\text{calc}}(T_{\text{exp}}, H_{\text{exp}}) \times T$ curves for any applied magnetic field. For FOM, the following expressions are proposed:

$$M^*(T, H) = \frac{M_x(T, H) - M_{\min}(H)}{M_{\max}(H) - M_{\min}(H)} \quad (8)$$

$$M^t(T, H) = \text{sech} \left[\exp \left(\frac{\pi}{2} M^*(T, H) \right) \right] \quad (9)$$

$$M^t(T, H) = a_0(H) + \frac{a_1(H)}{\pi} \arctan \left[\left(\frac{T - a_2(H)}{a_3(H)} \right) + \frac{\pi}{2} \right] \quad (10)$$

where Eq. 10 is the Gaussian Cumulative distribution⁴² and $a_0(H)$ to $a_3(H)$ are field-dependent constants. Notice that a single fitting equation was not effective when applied directly to $M_{\text{calc}}(T_{\text{exp}}, H_{\text{exp}})$. Thus, it was necessary to calculate a dimensionless variable (M^*) first, making $M_x = M_{\text{calc}}$, followed by a variable transformation (M^t) using Eq. 9. Then, Eq. 10 was applied to M^t to find $a_0(H)$ to $a_3(H)$.

In Eq. 8, M_x can be an experimental or calculated magnetization (from Eq. 7). Also, $M_{\min}(H)$ and $M_{\max}(H)$ are the minimum and maximum magnetizations, whose values at intermediate fields are obtained from interpolation.

Next, in Step 8, the field-dependent constants, $a_0(H)$ to $a_3(H)$, are interpolated (using linear, quadratic or cubic polynomials) to determine their values at intermediates fields. The new set of interpolated field-dependent constants are re-inserted in Eqs. 10 to 8, in that order, making $M_x = M_{\text{fit}}$ to produce the magnetization curves at intermediate fields, as illustrated in Fig. 3(a). In Section III A, Fig. 7(b) shows the magnetization curves for $\text{La(Fe,Mn,Si)}_{13}\text{H}_y$.

For SOM, Step 6 is identical and Eq. 7 is used to obtain the so-called $M_{\text{calc}}(T_{\text{exp}}, H_{\text{exp}}) \times T$ curves for all baseline applied magnetic fields. In Step 7, a Boltzmann (or reverse) Sigmoid function given by⁴²,

$$M(T, H) = a_0(H) + \frac{a_1(H)}{1 + \exp \left[- \left(\frac{T - a_2(H)}{a_3(H)} \right) \right]} \quad (11)$$

is applied directly to $M_{\text{calc}}(T_{\text{exp}}, H_{\text{exp}})$ to determine the field-dependent constants $a_0(H)$ to $a_3(H)$, as seen in Fig. 3(b).

Next, to evaluate if the magnetization fitting can reproduce the ΔS_T derived from the experimental specific heat capacity data as satisfactorily as the $T - s$ diagram (Eq. 5), additional verification is performed in Step 9. The ΔS_T from magnetization data is calculated from^{8,37}:

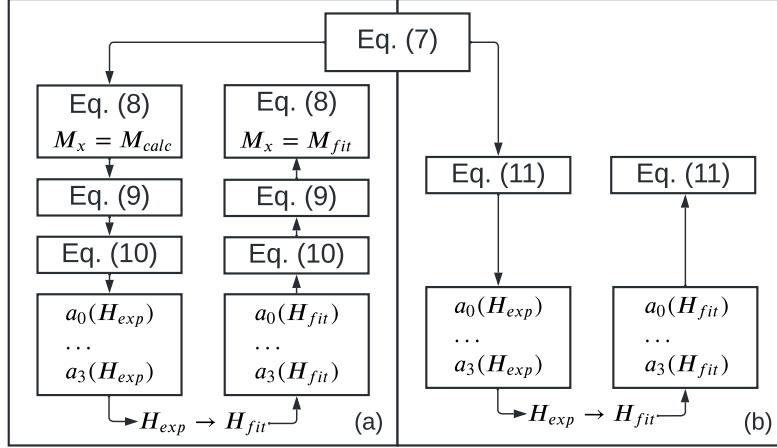


FIG. 3. Steps 7 and 8 of the data fitting algorithm. Calculation of the magnetization curves at intermediate fields: (a) FOM; (b) SOM.

$$\Delta S_T = \int_{H_i}^{H_f} \left(\frac{\partial M}{\partial T} \right) dH \quad (12)$$

Figure 8 compares the two ΔS_T results for $\text{La(Fe,Mn,Si)}_{13}\text{H}_y$ FOM. Although this step is not mandatory, it assures the quality and consistency of the fitting routine.

Lastly, in Step 10, the algorithm organizes the fitted data (specific heat, entropy, MCE and magnetization) as a function of temperature and intermediate fields in output files. These files can be used in mathematical models to simulate thermomagnetic conversion systems such as active magnetic regenerators and thermomagnetic motors/generators.

III. RESULTS AND DISCUSSIONS

A. $\text{La(Fe,Mn,Si)}_{13}\text{H}_y$ FOM

Figure 4(a) presents the experimental specific heat capacity data (open symbols) for a $\text{La(Fe,Mn,Si)}_{13}\text{H}_y$ alloy with $T_{trans} \approx 297$ K⁴³. The temperature and magnetic field range from 270 to 320 K (0.1-K increments) and 0 to 1.5 T (0.5-T increments). Since this material presents minimal thermal hysteresis, an average value of the heating and cooling curves is considered. As will be discussed further, the algorithm can predict the heating and cooling curves that characterize hysteretic FOM.

As can be seen from Fig. 4(a), the temperature range is quite extensive, and there is some

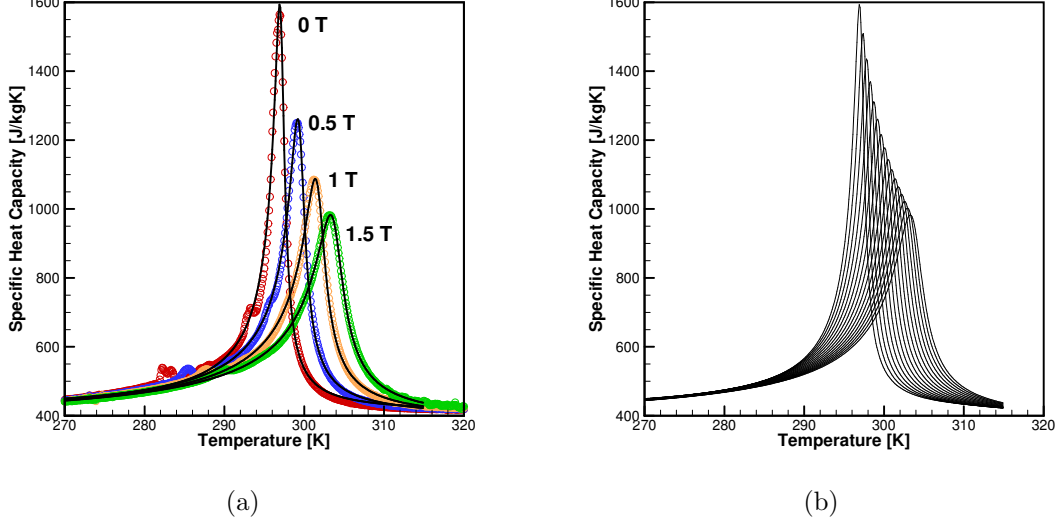


FIG. 4. $\text{La(Fe,Mn,Si)}_{13}\text{H}_y$ $c(T, H) \times T$ curves: (a) experimental data (open symbols) and curves fitted to the data using Eq. 1 (solid lines); (b) calculated specific heat capacity at intermediate fields from 0 to 1.5 T (0.1-T increments).

noise in the input data. Thus, the data were treated before Step 2 to improve the fitting quality. More specifically, the 5-K range at the end of the interval was cut out. Thus, the fitting is valid from 270 to 315 K. Figure 4(a) also presents the curves fitted to the baseline (experimental) applied magnetic fields (solid black lines). Figure 4(b) shows the calculated specific heat capacities at the intermediate fields between 0 and 1.5 T (0.1-T increments).

The Root Mean Square Error (RMSE) for the specific heat capacity was evaluated at different applied magnetic fields as follows: (i) at 0 T, $\text{RMSE} = 17.5 \text{ J/kg.K}$ (4.2% of the minimum and 1.1% of the peak values); (ii) at 0.5 T, $\text{RMSE} = 9.4 \text{ J/kg.K}$ (2.2% of the minimum and 0.8% of the peak values); (iii) at 1 T, $\text{RMSE} = 6.6 \text{ J/kg.K}$ (1.5% of the minimum and 0.6% of the peak values); and (iv) at 1.5 T, $\text{RMSE} = 5.0 \text{ J/kg.K}$ (1.2% of the minimum and 0.5% of the peak values). The RMSE results showed that the deviations between the fitted curves and the experimental data are small, decreasing as the applied field increases. This demonstrates the robustness of the proposed correlating procedure as well the quality of the adjustment of the Pearson type IV (Eq. 1) over the specific heat data for FOM (also observed in Fig. 11(a) in the next section). In Fig. 4(a), even in the presence of some noise on the measured data, the fitting was quite good capturing well the peak and trends of the experimental data.

Figure 5 presents the $T - s$ diagram for $\text{La(Fe,Mn,Si)}_{13}\text{H}_y$ obtained from Eq. 4 using

the calculated specific heat capacities at the intermediate fields shown in Fig. 4(b). The temperature and applied magnetic field range from 270 to 315 K (0.1-K increments) and 0 to 1.5 T (0.1-T increments).

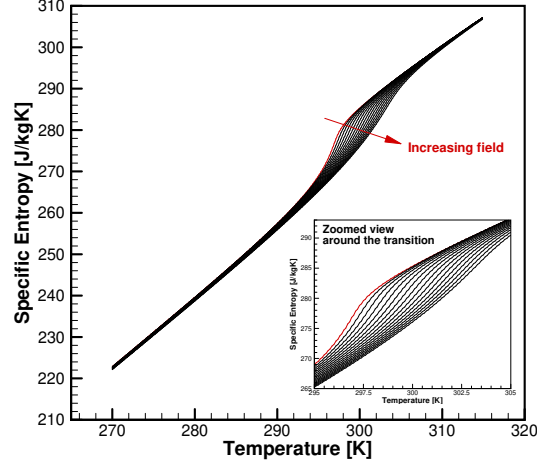


FIG. 5. $\text{La(Fe,Mn,Si)}_{13}\text{H}_y$ $T - s$ diagram from the predicted $c(T, H)$ data to intermediate fields from 0 to 1.5 T, in increments of 0.1 T.

From the $T - s$ in Fig. 5, one can calculate the main parameters associated with the magnetocaloric effect and compare them with the experimental data. For $\text{La(Fe,Mn,Si)}_{13}\text{H}_y$, Fig. 6(a) shows the calculated ΔS_T together with the data measured at the baseline applied magnetic fields. Figure 6(b), in turn, presents the results interpolated at the intermediate fields. Figure 6(c) and (d) present the corresponding results associated with ΔT_{ad} . The open symbols represent the experimental data and the solid lines are the correlation results.

The RMSE for the isothermal entropy change was evaluated at different applied fields: (i) at 0.5 T, RMSE = 0.20 J/kg.K (3.3% of the peak value); (ii) at 1 T, RMSE = 0.27 J/kg.K (3.1% of the peak value); (iii) at 1.5 T, RMSE = 0.3 J/kg.K (3.0% of the peak value). Analogously, for the adiabatic temperature change the RMSE are as follows: (i) at 0.5 T, RMSE = 0.10 K (6.6% of the peak value); (ii) at 1 T, RMSE = 0.14 K (4.7% of the peak value); (iii) at 1.5 T, RMSE = 0.15 J/kg.K (3.9% of the peak value). In practice, considering that a FOM is designed to operate around the peak MCE value, one can conclude that the correlation results are reliable. However, some differences are observed in the range $280 \leq T \leq 295$ K where the model under predicts the experimental data. This is the same region where the noise is observed in the specific heat capacity data (see Fig. 4(a)), and indicates the necessity to use high quality experimental data. Notice also that the last 5 K

of the temperature interval had to be cut out in order to improve the fitting quality.

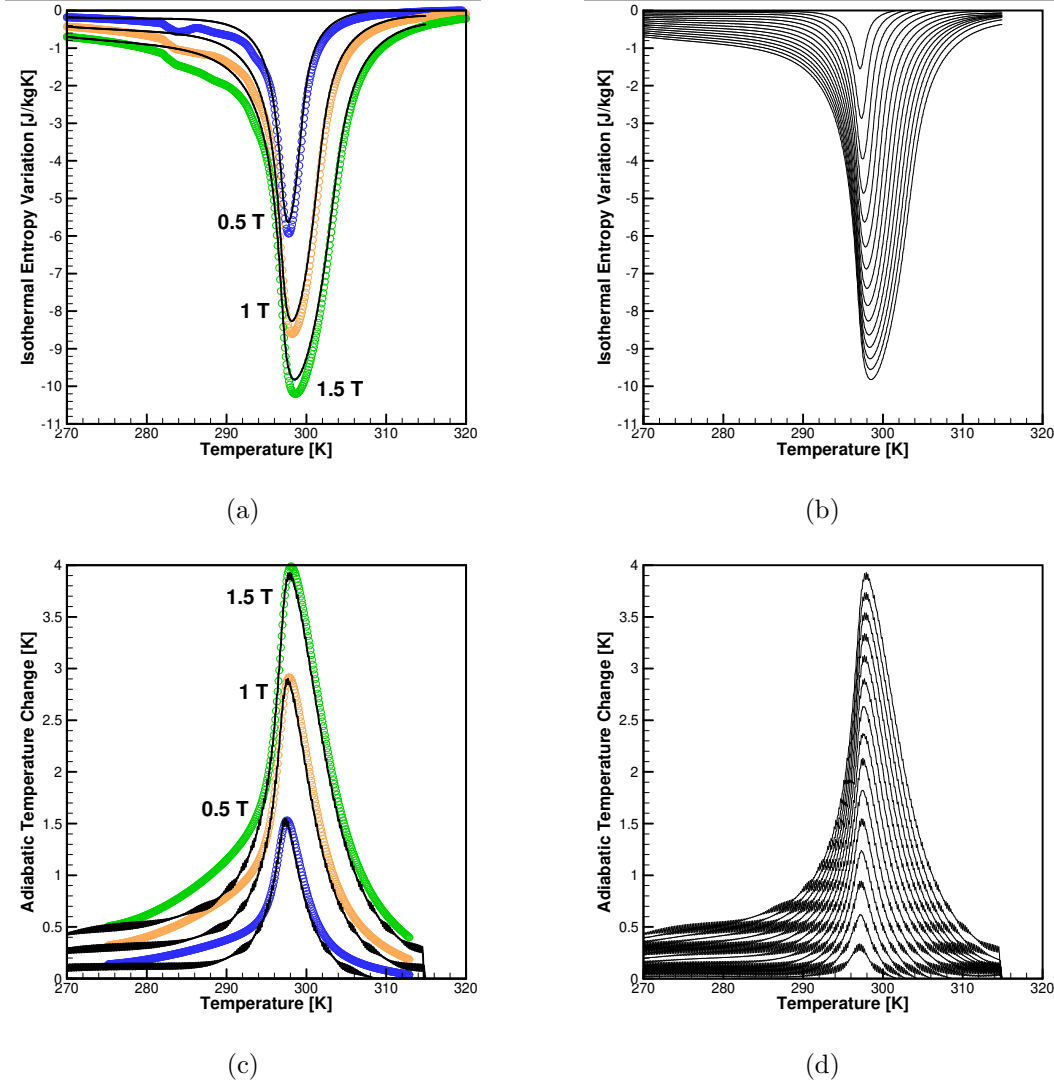


FIG. 6. Magnetocaloric properties of $\text{La}(\text{Fe,Mn,Si})_{13}\text{H}_y$: (a) ΔS_T experimental data (open symbols) and calculated values (solid lines) at the baseline applied magnetic fields; (b) calculated ΔS_T at intermediate fields from 0 to 1.5 T (0.1-T increments); (c) ΔT_{ad} experimental data (open symbols) and calculated values (solid lines) at the baseline applied magnetic fields; (d) calculated ΔT_{ad} at intermediate fields from 0 to 1.5 T (0.1-T increments).

The $T - s$ data for the baseline fields (0, 0.5, 1.0 and 1.5 T) can also be used in Eq. 7 to obtain $M_{\text{calc}}(T_{\text{exp}}, H_{\text{exp}})$. For $\text{La}(\text{Fe,Mn,Si})_{13}\text{H}_y$, having experimental data for M_0 at all baseline fields, and at temperatures ranging from 310 K to 320 K, may be necessary since some data points may need to be discarded. Recall that in Fig. 4(a) the upper temperature limit was reduced from 320 K to 315 K. Thus, M_0 was evaluated at 315 K to construct

the magnetization curve using Eq. 7. Figure 7(a) presents the $M_{\text{calc}}(T_{\text{exp}}, H_{\text{exp}})$ results and Fig. 7(b) shows the calculated magnetization curves in the 0 to 1.5 T interval, with 0.1-T increments.

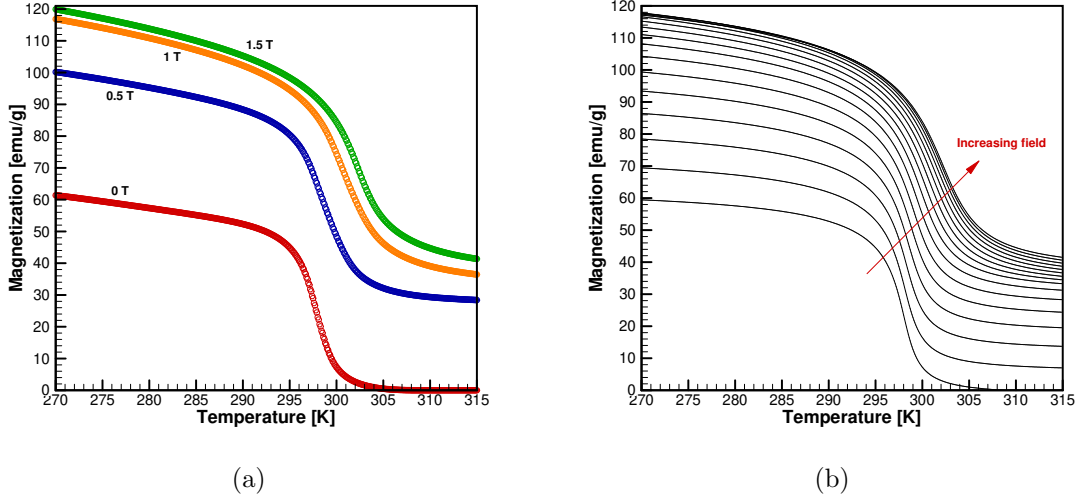


FIG. 7. $M(T, H) \times T$ curves for $\text{La}(\text{Fe}, \text{Mn}, \text{Si})_{13}\text{H}_y$: (a) $M_{\text{calc}}(T_{\text{exp}}, H_{\text{exp}})$ calculated from Eq. 7; (b) magnetization calculated from Eqs. 8-10 at intermediate applied magnetic fields from 0 to 1.5 T (0.1-T increments).

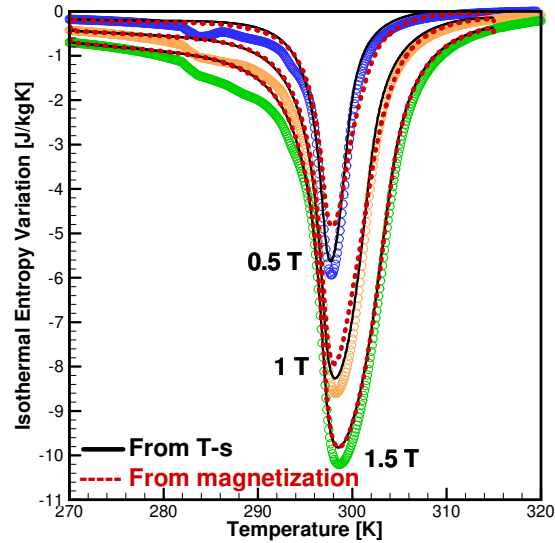


FIG. 8. ΔS_T comparison between experimental data (open symbols) and calculations from the $T-s$ diagram (black solid lines) and magnetization data (Eq. 12) (red dashed lines) for $\text{La}(\text{Fe}, \text{Mn}, \text{Si})_{13}\text{H}_y$.

Finally, Fig. 8 compares the ΔS_T calculated from the $T-s$ diagram (black solid lines),

Eq. 12 (red dashed lines), and the experimental data (open symbols) for $\text{La}(\text{Fe,Mn,Si})_{13}\text{H}_y$. The RMSE for ΔS_T obtained from the magnetization data are as follows: (i) at 0.5 T, RMSE = 0.28 J/kg.K (4.7% of the peak value); (ii) at 1 T, RMSE = 0.35 J/kg.K (4.0% of the peak value); (iii) at 1.5 T, RMSE = 0.3 J/kg.K (3.0% of the peak value). Although the RMSE have some increasing in respect to the $T - s$ diagram results, the procedure proved to be reliable and the magnetization data calculated from Eq. 7 and Eqs. 8-10 are in accordance with the expected ranges and trends. For FOM, as in Fig. 7 (and Figs. 9-10 in the next section), the expected abrupt magnetization variation is observed.

B. $\text{MnFeP}_x\text{As}_{1-x}$ FOM with hysteresis

In this section, the proposed algorithm is applied to experimental data for a $\text{MnFeP}_x\text{As}_{1-x}$ first-order hysteretic material. The hysteresis was characterized through measurements of the specific heat capacity following heating and cooling protocols⁴⁴. The temperature ranges from 250 to 300 K (0.1-K increments), while the applied magnetic field varies between 0 and 1.5 T, in steps of 0.5 T. The peak specific heat capacity at 0 T is observed at around 272.8 K for the cooling curve and around 275 K for the heating curve.

Figure 9(a) presents the experimental specific heat capacity data (open symbols) and the fitted curve from Eq. 1 (black solid lines). Notice that only the curves for 0 and 1.5 T are presented to improve the visualization of the thermal hysteresis. From the proposed equations, it is possible to obtain the $T - s$ diagram, presented in Fig. 9(b), and the $M \times T$ curves, in Fig. 9(c), for the cooling (in blue) and heating (in red) procedures.

The results confirm the expected thermal hysteresis behavior^{9,44}. Thus, the fitting procedure is effective at correlating the thermomagnetic parameters at intermediate fields for both heating and cooling curves, capturing well the peak, trends and differences between the heating and cooling protocols observed in the experimental data. This is also demonstrated by evaluating the RMSE for the specific heat capacity: (i) at 0 T-cooling, RMSE = 17.9 J/kg.K (3.5% of the minimum and 0.9% of the peak values); (ii) at 0 T-heating, RMSE = 19.45 J/kg.K (3.8% of the minimum and 0.9% of the peak values); (iii) at 1.5 T-cooling, RMSE = 18.73 J/kg.K (3.7% of the minimum and 0.9% of the peak values); and (iv) at 1.5 T-heating, RMSE = 18.47 J/kg.K (3.7% of the minimum and 0.8% of the peak values).

Considering only the heating process for brevity, Fig. 10 presents the $c(T, H) \times T$ curves,

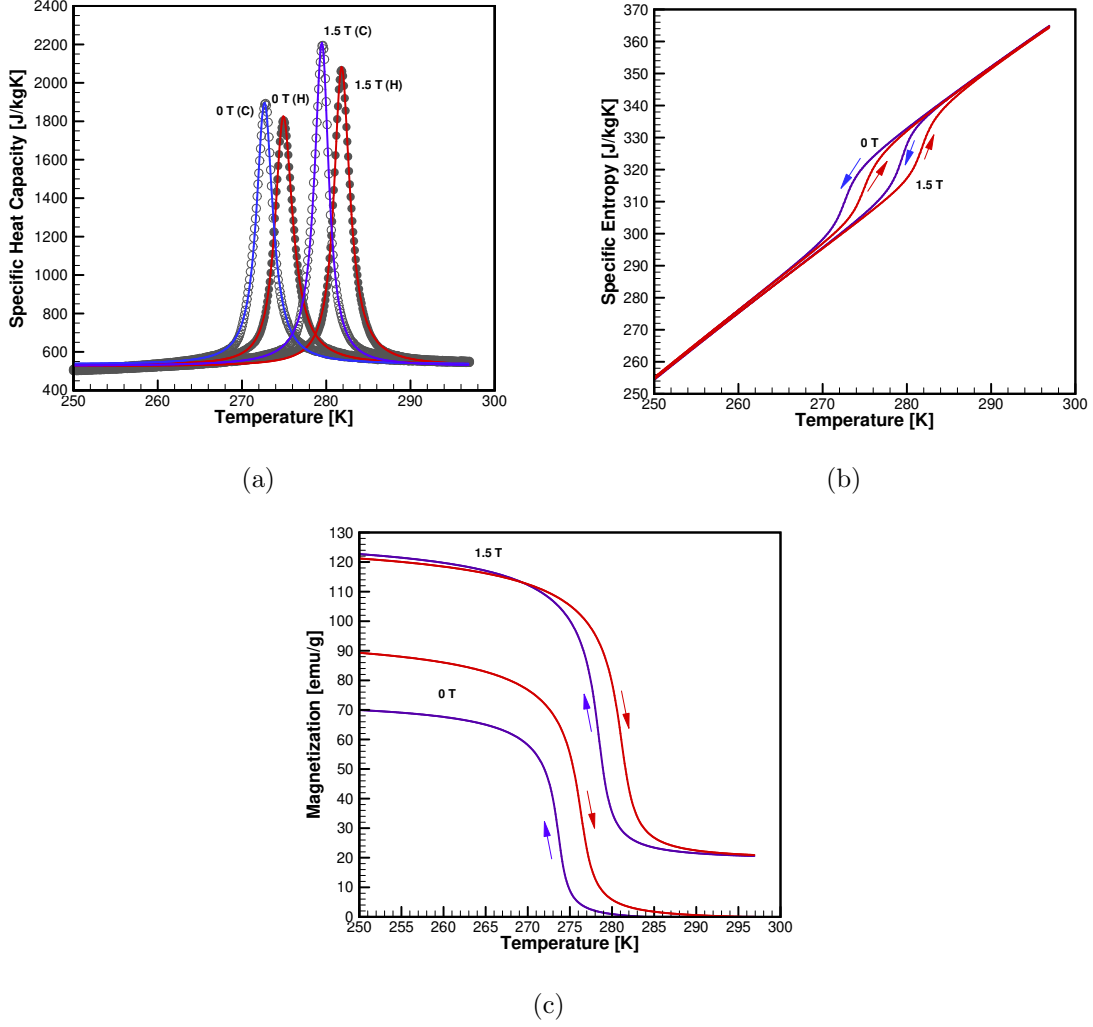


FIG. 9. $\text{MnFeP}_x\text{As}_{1-x}$ results at 0 and 1.5 T for heating (red) and cooling (blue) processes, demonstrating the presence of thermal hysteresis: (a) $c(T, H) \times T$ curves comparing experimental data (symbols) and fitted curve from Eq. 1 (solid lines); (b) predicted $T - s$ diagram from Eq. 4; (c) predicted $M \times T$ curves from Eqs. 8-10.

$T - s$ diagram and $M \times T$ behavior for fields between 0 and 1.5 T, in steps of 0.1 T. Also, Fig. 11(a) compares the ΔS_T calculations with the experimental data, and Fig. 11(b) presents the correlation results for intermediate fields, derived from the $T - s$ diagram shown in Fig. 10(b).

The RMSE values for the isothermal entropy change are as follows: (i) at 0.5 T, RMSE = 0.14 J/kg.K (1.6% of the peak value); (ii) at 1 T, RMSE = 0.21 J/kg.K (1.6% of the peak value); (iii) at 1.5 T, RMSE = 0.26 J/kg.K (1.8% of the peak value). Comparing Figs. 6(a) and 11(a) and the RMSE, the $\text{MnFeP}_x\text{As}_{1-x}$ correlating procedure presented slightly higher

quality results than $\text{La}(\text{Fe,Mn,Si})_{13}\text{H}_y$, which can be possibly associated with the use of input specific heat capacity data with less noise.

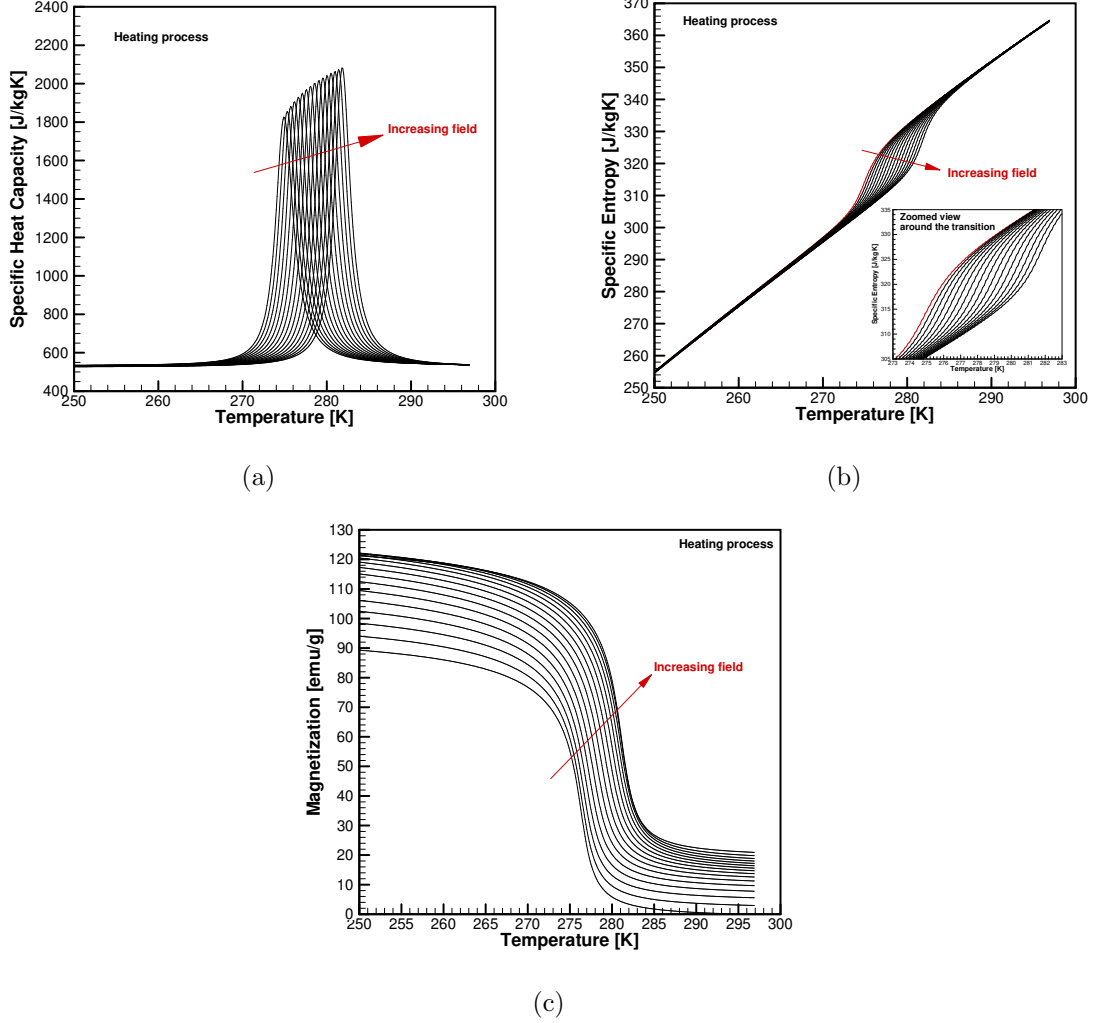


FIG. 10. $\text{MnFeP}_x\text{As}_{1-x}$ fitting results from 0 to 1.5 T, in increments of 0.1 T, considering only the heating process: (a) $c(T, H) \times T$ curves; (b) $T - s$ diagram; (c) $M \times T$ curves.

C. Gd and GdY-alloys

Lastly, the fitting algorithm is applied to SOM data for Gd^{45} and $\text{Gd}_{94.79}\text{Y}_{5.21}$ (or simply GdY)²², for which T_{trans} are around 290 and 270 K, respectively. For Gd, the temperature data range from 260 to 314 K, while for the GdY data the range is from 243 to 309 K, in steps of 1 K. The experimental magnetic fields vary between 0 and 2.0 T, in steps of 0.5 T.

Figure 12(a) presents the experimental specific heat capacity data (symbols) and the fitted

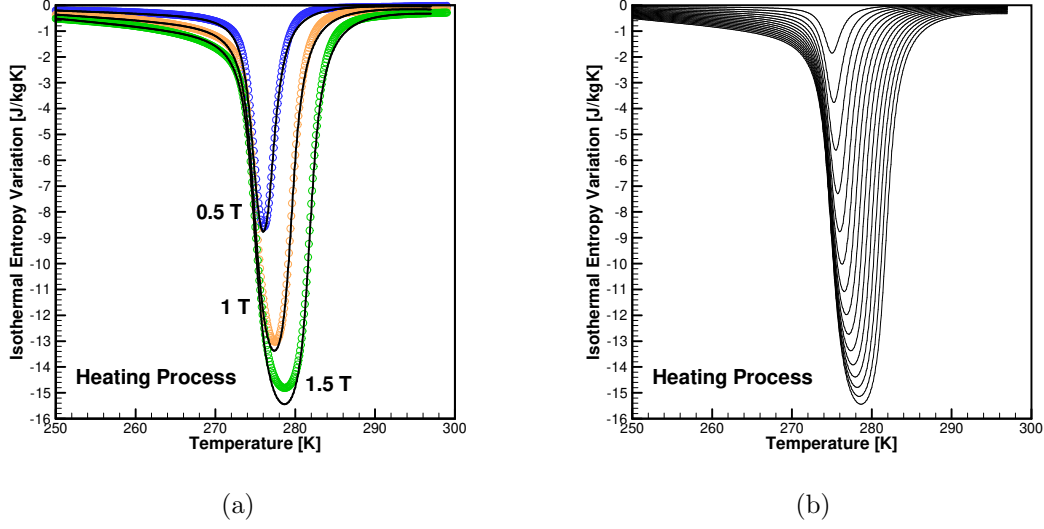


FIG. 11. $\text{MnFeP}_x\text{As}_{1-x}$ ΔS_T results considering the heating process: (a) comparison between experimental data (open symbols) and correlation (solid lines) for the baseline fields; (b) fitting results for intermediate fields from 0 to 1.5 T, in increments of 0.1 T.

curve from Eqs. 2-3 (solid black lines), while Fig. 12(b) shows the corresponding calculated values at intermediate fields, from 0 to 2 T, in increments of 0.1 T. Notice that, as previously explained, since for SOM the fitting curves are polynomials, some temperature ranges must be cut out to remove oscillations. Hence, for Gd and GdY, the fitted temperatures range from 260 to 310 K and 243 to 300 K, respectively, with steps of 0.1 K.

In this section, the RMSE will be evaluated only for applied fields greater than or equal to 0.5 T. Thus, the Gd specific heat capacity values are as follows: (i) at 0.5 T, RMSE = 0.51 J/kg.K (0.21% of the minimum and 0.16% of the peak values); (ii) at 1 T, RMSE = 0.14 J/kg.K (0.06% of the minimum and 0.05% of the peak values); (iii) at 1.5 T, RMSE = 0.29 J/kg.K (0.11% of the minimum and 0.09% of the peak values); and (iv) at 2 T, RMSE = 0.33 J/kg.K (0.12% of the minimum and 0.11% of the peak values). The corresponding values for the GdY-alloy are: (v) at 0.5 T, RMSE = 0.60 J/kg.K (0.28% of the minimum and 0.20% of the peak values); (vi) at 1 T, RMSE = 0.56 J/kg.K (0.25% of the minimum and 0.19% of the peak values); (vii) at 1.5 T, RMSE = 0.48 J/kg.K (0.21% of the minimum and 0.17% of the peak values); and (viii) at 2 T, RMSE = 0.36 J/kg.K (0.15% of the minimum and 0.13% of the peak values). The specific heat prediction for SOM, if in one hand, the model quality is reduced at low fields (from 0 T up to 0.5 T) due to the impossibility to find a single equation to be adjusted over the zero and the intermediate-field data. As a

consequence, the predicted magnetocaloric effect, showed next in Fig. 14(b) are less accurate at low fields. On the other hand, to the fields higher than 0.5 T the model did a quite good job in reproducing experimental data for specific heat, presenting the lowest RMSE values. Hence, Eqs. 2-3 are very accurate on predicting specific heat capacity.

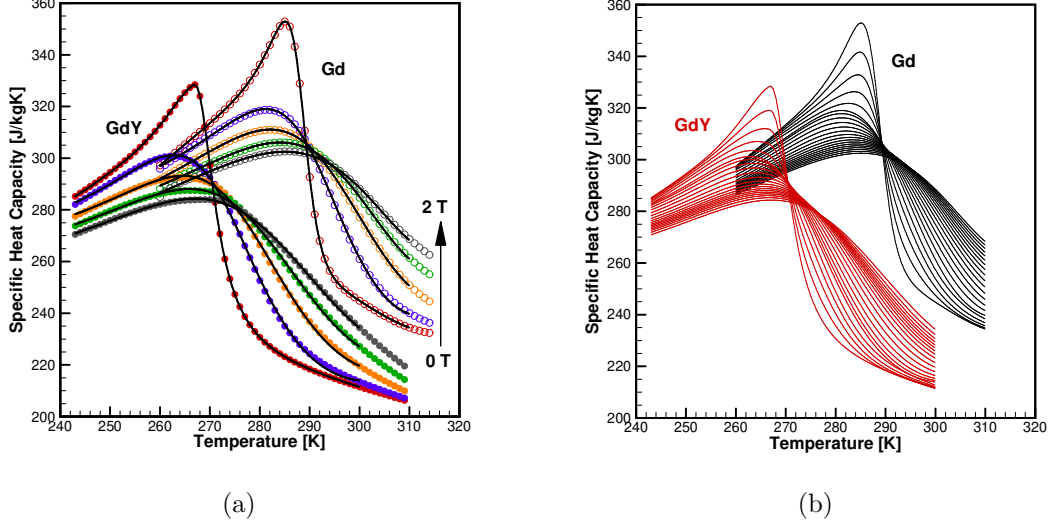


FIG. 12. $c(T, H) \times T$ curves for Gd and $\text{Gd}_{94.79}\text{Y}_{5.21}$: (a) experimental data (open symbols - Gd, solid symbols - GdY) and fitted curve from Eqs. 2-3 (solid lines) for the baseline fields; (b) calculated specific heat capacities for intermediate fields between 0 and 2.0 T, in steps of 0.1 T.

From the results shown in Fig. 12(b), one can build the $T - s$ diagrams of Fig. 13, from which ΔT_{ad} and ΔS_{T} can be evaluated. Figure 14(a) shows a comparison of the calculated ΔS_{T} and the experimental data for the baseline applied magnetic fields, while Fig. 14(b) presents the correlation results at intermediate fields between 0 and 2.0 T in steps of 0.1 T.

The RMSE values for the isothermal entropy change are evaluated, for Gd, as follows: (i) at 0.5 T, RMSE = 0.13 J/kg.K (9.8% of the peak value); (ii) at 1 T, RMSE = 0.06 J/kg.K (2.1% of the peak value); (iii) at 1.5 T, RMSE = 0.10 J/kg.K (2.8% of the peak value); (iv) at 2 T, RMSE = 0.06 J/kg.K (1.4% of the peak value). For GdY, the RMSE are slightly better: (v) at 0.5 T, RMSE = 0.03 J/kg.K (2.3% of the peak value); (vi) at 1 T, RMSE = 0.03 J/kg.K (1.1% of the peak value); (vii) at 1.5 T, RMSE = 0.03 J/kg.K (0.8% of the peak value); (viii) at 2 T, RMSE = 0.01 J/kg.K (0.1% of the peak value). Comparing the RMSE results for Gd and GdY, the input specific heat data were provided by different sources, and hence, the higher accurate results for the correlating procedure observed to GdY may be related to the input data quality. Additionally, it is expected that the peak MCE for Gd

would be higher than the GdY allow, however, this may also be related to the Gd lower quality grade of the sample measured.

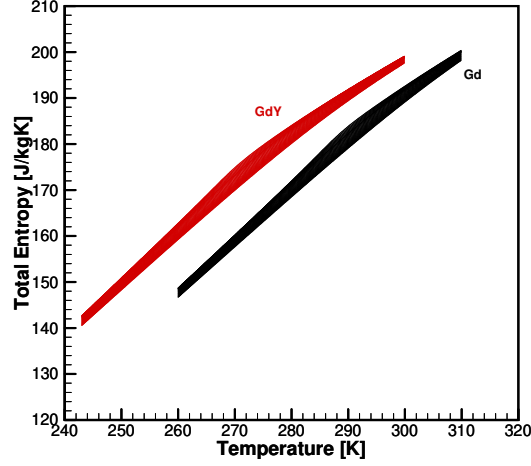


FIG. 13. $T - s$ diagrams for Gd and $\text{Gd}_{94.79}\text{Y}_{5.21}$ from the calculated $c(T, H)$ data at intermediate fields between 0 and 2.0 T, in steps of 0.1 T.

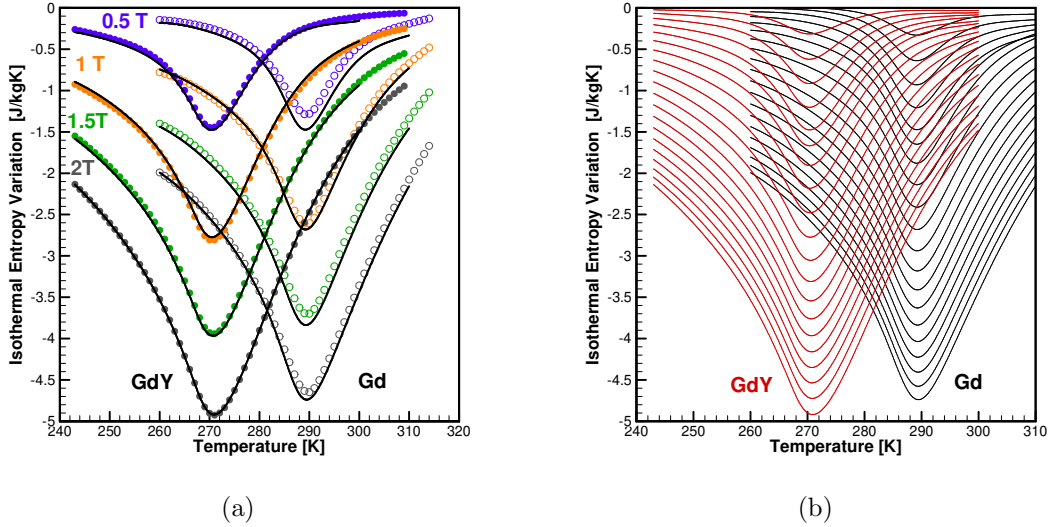


FIG. 14. Isothermal entropy change for Gd and $\text{Gd}_{94.79}\text{Y}_{5.21}$: (a) ΔS_T experimental data (open symbols - Gd, solid symbols - GdY) and calculated values (solid lines) at the baseline fields; (b) calculated ΔS_T at intermediate fields between 0 and 2.0 T, in steps of 0.1 T.

Figure 15 shows the magnetization results for SOM, where the $M_{\text{calc}}(T_{\text{exp}}, H_{\text{exp}})$ data are obtained from Eqs. 7 and III C. Notice that experimental magnetization data (not corrected for demagnetizing fields) were available and are, therefore, compared with the proposed

fitting in Figs. 15(a) and (b) for Gd and GdY, respectively. Figure 15(c) and (d) show the $M(T, H) \times T$ curves calculated from Eq. III C at intermediate fields from 0 to 2.0 T, in steps of 0.1 T. For SOM, a smooth phase change is observed in the magnetization experimental and calculated results.

The RMSE values of the magnetization for Gd are as follows: (i) at 0.5 T, RMSE = 10.26 emg/g (9.1% of the maximum value); (ii) at 1 T, RMSE = 1.21 emu/g (3.9% of the maximum value); (iii) at 1.5 T, RMSE = 0.84 emu/g (0.7% of the maximum value); (iv) at 2 T, RMSE = 0.5 emu/g (0.4% of the maximum value). For GdY the RMSE values are: (v) at 0.5 T, RMSE = 14.22 emg/g (11.6% of the maximum value); (vi) at 1 T, RMSE = 3.42 emg/g (2.6% of the maximum value); (vii) at 1.5 T, RMSE = 1.45 emg/g (1.1% of the maximum value); (viii) at 2 T, RMSE = 1.85 emg/g (1.33% of the maximum value). As can be observed in Fig. 15(a) and in accordance with the RMSE values, the deviations from the experimental data and the calculated magnetization are more significant at lower fields, where the data were not corrected for demagnetizing fields. Overall, a good reproduction of the magnetization data is observed at higher fields (> 0.5 T). For the 0.5 T, the prediction is more accurate at $T > T_{trans}$ (paramagnetic phase). This is because the specific heat capacity data (input) is not corrected for demagnetizing fields either, impacting on the predicted magnetization by Eq. 7. Therefore, the strategy to built the $M \times T$ curve in Eq. 7 starting from the highest temperature improves the precision of the predicted data even for the zero-field data. Again, if the magnetization experimental data are available, Eq. 7 is not necessary, and the intermediate fields data can be directly obtained from Eqs. 8-10 (FOM) or Eq. 11 (SOM).

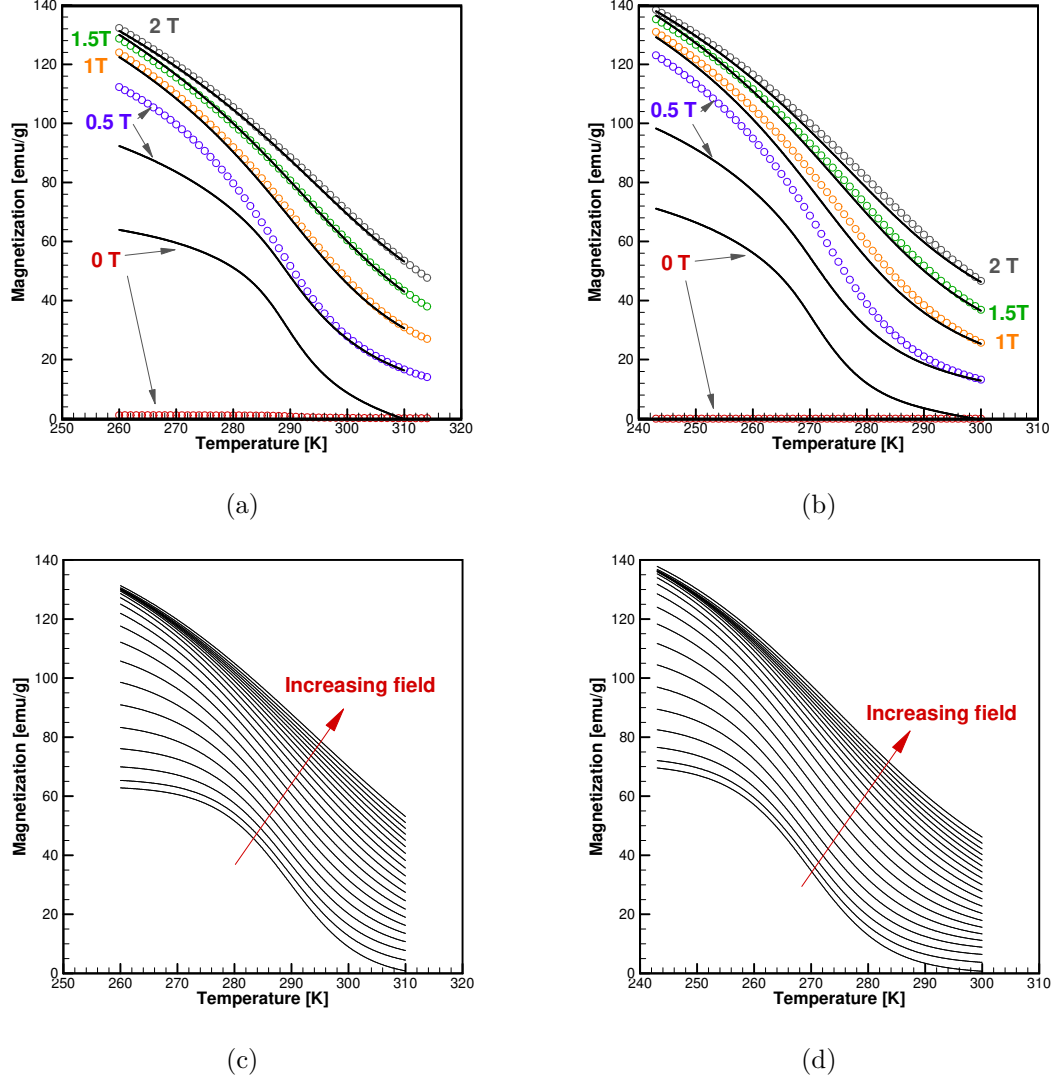


FIG. 15. $M_{\text{calc}}(T_{\text{exp}}, H_{\text{exp}}) \times T$ calculated from Eq. 7 compared with experimental data (open symbols): (a) Gd; (b) Gd_{94.79}Y_{5.21}. $M(T, H) \times T$ curves calculated from Eq. IIIC at intermediate fields between 0 and 2.0 T, in steps of 0.1 T: (c) Gd; (d) Gd_{94.79}Y_{5.21}.

CONCLUSION

This work proposed a fitting procedure to correlate the thermomagnetic properties and magnetocaloric effect of first- and second-order magnetocaloric materials as a function of temperature and applied magnetic field. The procedure comprises simple semi-empirical expressions whose primary input is experimental data for the specific heat capacity as a function of temperature at discrete magnetic fields (baseline data). Thermodynamically consistent equations are employed to derive expressions for entropy, magnetization and other relevant parameters, such as the isothermal entropy change and the adiabatic temperature change, at any field intensity and temperature within the baseline data range.

The routine, implemented in Python using cross-platform integrated development environment Spyder, is made available as a open-source code at https://github.com/lorenzosc/material_properties. The method was successfully tested for different first-order materials (FOM), $\text{La}(\text{Fe,Mn,Si})_{13}\text{H}_y$ and $\text{MnFeP}_x\text{As}_{1-x}$, and second-order materials (SOM), Gd and $\text{Gd}_{100-x}\text{Y}_x$.

For FOM, the specific heat capacity was successfully fitted by the Pearson type IV equation, which captured the data trend effectively, even with some noise in the baseline data. For SOM, the fitting was poorer at low fields, as no single equation could correlate the strong non-linearities observed at zero and intermediate fields. As a result, the magnetocaloric effect calculated at low fields (< 0.5 T) was less accurate. However, at fields higher than 0.5 T, the model reproduced the data for the specific heat capacity, ΔS_T and ΔT_{ad} with remarkable accuracy.

As expected, the fitting results for hysteretic FOM ($\text{MnFeP}_x\text{As}_{1-x}$) exhibited the expected behavior of a distinguished reversible region in the entropy diagram, different peak temperatures for the specific heat capacity and different transition temperatures for the magnetization curves⁴⁴.

The procedures to obtain the magnetization curves also proved reliable, as the expected abrupt magnetization changes typical of FOM and the smooth phase change characteristics of SOM were effectively captured by the models. The fitting for Gd and GdY was compared against experimental data (not corrected for demagnetizing fields), showing good performance at higher fields (> 0.5 T). For 0.5 T, however, the fitting is more accurate for $T > T_{\text{trans}}$ (paramagnetic phase). Additionally, the strategy to build the $M \times T$ curve

starting from the final temperature enhanced the precision of the predicted data even for the zero-field data.

As a final recommendation, only high-quality experimental data should be used as input to reduce physical inconsistencies and interpolations errors. The fitting performance at intermediate fields is greatly improved when at least four field intensities are used in the baseline data. Also, proper correction for demagnetizing fields helps improve the reliability of the predicted data.

ACKNOWLEDGEMENTS

The authors are grateful for the financial support from The National Institute of Science and Technology (Refrigeration and Thermophysics) through grants from Conselho Nacional de Desenvolvimento Científico e Tecnológico (CNPq 404023/2019-3) and Fundação de Amparo à Pesquisa e Inovação do Estado de Santa Catarina (FAPESC 2019TR0846). Financial support from Fundação de Amparo à Pesquisa do Estado de Minas Gerais (FAPEMIG) through Grant No. APQ-00877-21 (Demanda Universal) and Conselho Nacional de Desenvolvimento Científico e Tecnológico (CNPq) through Grant No. 405970/2021-8 is also acknowledged. The authors thank BASF (GER) for providing the $\text{MnFeP}_x\text{As}_{1-x}$ data used in this research paper.

REFERENCES

- ¹A. Kitanovski, J. Tusek, U. Tomc, U. Plaznik, M. Ozbolt, and A. Poredos, *Magnetocaloric Energy Conversion: From Theory to Applications* (Springer International Publishing, 2015).
- ²P. V. Trevizoli, T. V. Christiaan, P. Govindappa, I. Niknia, R. Teyber, J. R. Barbosa Jr., and A. Rowe, “Magnetic heat pumps: an overview of design principles and challenges,” *Science and Technology for the Built Environment* **22**, 507–519 (2016).
- ³R. A. Kishore and S. Priya, “A review on low-grade thermal energy harvesting: Materials, methods and devices,” *Materials* **11**, 1433 (2018).
- ⁴R. A. Kishore and S. Priya, “A review on design and performance of thermomagnetic devices,” *Renew. Sust. Energ. Rev.* **81**, 33–44 (2018).
- ⁵A. Greco, C. Aprea, A. Maiorino, and C. Masselli, “A review of the state of the art of solid-state caloric cooling processes at room-temperature before 2019,” *International Journal of Refrigeration* **106**, 66–88 (2019).
- ⁶K. K. Nielsen, J. Tusek, K. Engelbrecht, S. Schopfer, A. Kitanovski, C. R. H. Bahl, A. Smith, N. Pryds, and A. Poredos, “Review on numerical modeling of active magnetic regenerators for room temperature applications,” *Int. J. Refrig.* **34**, 603–616 (2011).
- ⁷J. Eustache, A. Plait, F. Dubas, and R. Glises, “Review of multi-physics modeling on the active magnetic regenerative refrigeration,” *Math. Comput. Appl.* **26**, 47 (2021).
- ⁸V. K. Pecharsky, K. A. Gschneidner, Jr., A. O. Pecharsky, and A. M. Tishin, “Thermodynamics of the magnetocaloric effect,” *Phys. Rev. B* **64**, 144406(1–13) (2001).
- ⁹O. Gutfleisch, T. Gottschall, M. Fries, D. Benke, I. Radulov, K. P. Skokov, H. Wende, M. Gruner, M. Acet, P. Entel, and M. Farle, “Mastering hysteresis in magnetocaloric materials,” *Phil. Trans. R. Soc. A* **374**, 20150308 (2016).
- ¹⁰J. Lyubina, “Magnetocaloric materials for energy efficient cooling,” *J. Phys. D: Appl. Phys.* **50**, 053002 (2017).
- ¹¹T. Gottschall, K. P. Skokov, M. Fries, A. Taubel, I. Radulov, F. Scheibel, D. Benke, S. Riegg, and O. Gutfleisch, “Making a cool choice: The materials library of magnetic refrigeration,” *Advanced Energy Materials* **9**, 1901322 (2019).
- ¹²S. Jacobs, J. Auringer, A. Boeder, J. C. and L Komorowski, J. Leonard, S. Russek, and C. Zimm, “The performance of a large-scale rotary magnetic refrigerator,” *Int. J. Refrig.*

- 37**, 84–91 (2014).
- ¹³T. Lei, K. Engelbrecht, K. K. Nielsen, N. N. Bez, and C. R. H. Balh, “Study of multi-layer active magnetic regenerators using magnetocaloric materials with first and second order phase transition,” J. Phys. D: Appl. Phys. **49**, 345001 (2016).
 - ¹⁴R. Teyber, P. V. Trevizoli, T. V. Christiaanse, P. Govindappa, I. Niknia, and A. Rowe, “Performance evaluation of two-layer active magnetic regenerators with second-order magnetocaloric materials,” Appl. Therm. Eng. **106**, 405–414 (2016).
 - ¹⁵P. Govindappa, P. V. Trevizoli, O. Campbel, I. Niknia, T. V. Christiaanse, R. Teyber, and A. Rowe, “Experimental investigation on $\text{MnFeP}_{1-x}\text{As}_x$ multilayer active magnetic regenerators,” J. Phys. D: Appl. Phys. **50**, 315001 (2017).
 - ¹⁶V. K. Pecharsky and K. A. Gschneidner, Jr., “Giant magnetocaloric effect in $\text{Gd}_5\text{Ge}_2\text{Si}_2$,” Phys. Rev. Lett. **78**, 4494–4497 (1997).
 - ¹⁷S. Y. Dan’kov, A. M. Tishin, V. K. Pecharsky, and K. A. Gschneidner, Jr., “Magnetic phase transitions and the magnetothermal properties of gadolinium,” Phys. Rev. B **57**, 3478–3490 (1998).
 - ¹⁸O. Tegus, E. Brück, K. H. J. Buschow, and F. R. de Boer, “Transition-metal-based magnetic refrigerants for room-temperature applications,” Nature **415**, 150–152 (2002).
 - ¹⁹R. Bjørk, C. R. H. Bahl, A. Smith, and N. Pryds, “Review and comparison of magnet designs for magnetic refrigeration,” Int. J. Refrig. **33**, 437–448 (2010).
 - ²⁰J. Lozano, K. Engelbrecht, C. Bahl, K. Nielsen, J. Barbosa, A. Prata, and N. Pryds, “Experimental and numerical results of a high frequency rotating active magnetic refrigerator,” Int. J. Refrig. **37**, 92–98 (2014).
 - ²¹V. Basso, M. Küpferling, C. Curcio, C. Bennati, A. Barzca, M. Katter, M. Bratko, E. Lovell, J. Turcaud, and L. F. Cohen, “Specific heat and entropy change at the first order phase transition of $\text{La}(\text{Fe-Mn-Si})_{13-\text{H}}$ compounds,” J. Appl. Phys. **118**, 053907 (2015).
 - ²²H. N. Bez, A. T. Nakashima, G. B. Lang, B. S. de Lima, A. J. Machado, J. A. Lozano, and J. R. Barbosa, “Performance assessment and layer fraction optimization of Gd-Y multilayer regenerators for near room-temperature magnetic cooling,” International Journal of Air-Conditioning and Refrigeration **28**, 2050027 (2020).
 - ²³B. C.P. and R. D.S., “Magnetic disorder as a first-order phase transformation,” Physical Review **126**, 104 – 115 (1962).
 - ²⁴A. Morrish, *The Physical Principles of Magnetism* (John Wiley & Sons, Inc., 1965).

- ²⁵V. Franco, J. Blázquez, B. Ingale, and A. Conde, “The magnetocaloric effect and magnetic refrigeration near room temperature: Materials and models,” *Annual Review of Materials Research* **42**, 305–342 (2012).
- ²⁶V. Franco, J. Blázquez, J. Ipus, J. Law, L. Moreno-Ramírez, and A. Conde, “Magnetocaloric effect: From materials research to refrigeration devices,” *Progress in Materials Science* **93**, 112–232 (2018).
- ²⁷M. Risser, C. Vasile, B. Keith, T. Engel, and C. Muller, “Construction of consistent magnetocaloric materials data for modelling magnetic refrigerators,” *International Journal of Refrigeration* **35**, 459–467 (2012).
- ²⁸I. Niknia, P. V. Trevizioli, T. V. Christianse, P. Govindappa, R. Teyber, and A. Rowe, “Material screening metrics and optimal performance of an active magnetic regenerator,” *J. Appl. Phys.* **121**, 064902 (2017).
- ²⁹I. Niknia, P. V. Trevizoli, P. Govindappa, T. V. Christiaanse, R. Teyber, and A. Rowe, “Multiple points of equilibrium for active magnetic regenerators using first order magnetocaloric material,” *Journal of Applied Physics* **123**, 204901 (2018).
- ³⁰T. Hess, C. Vogel, L. Maier, A. Barcza, H. Vieyra, O. Schäfer-Welsen, J. Wöllenstein, and K. Bartholomé, “Phenomenological model for a first-order magnetocaloric material,” *International Journal of Refrigeration* **109**, 128–134 (2020).
- ³¹A. Maiorino, M. G. Del Duca, U. Tomc, J. Tušek, A. Kitanovski, and C. Aprea, “A numerical modelling of a multi-layer lafecosi active magnetic regenerator by using artificial neural networks,” *Applied Thermal Engineering* **197**, 117375 (2021).
- ³²L. Paixão, E. Usuda, W. Imamura, and A. Carvalho, “High-field specific heat and entropy obtained from adiabatic temperature change,” *The European Physical Journal Plus* **136**, 1–9 (2021).
- ³³V. K. Pecharsky and K. A. Gschneidner, Jr., “Magnetocaloric effect from indirect measurements: magnetization and heat capacity,” *J. Appl. Phys.* **86**, 565–575 (1999).
- ³⁴L. Moreno-Ramírez, V. Franco, A. Conde, H. Neves Bez, Y. Mudryk, and V. Pecharsky, “Influence of the starting temperature of calorimetric measurements on the accuracy of determined magnetocaloric effect,” *Journal of Magnetism and Magnetic Materials* **457**, 64–69 (2018).
- ³⁵K. Pearson and O. M. F. E. Henrici, “X. contributions to the mathematical theory of evolution.—ii. skew variation in homogeneous material,” *Philosophical Transactions*

- of the Royal Society of London. (A.) **186**, 343–414 (1895).
- ³⁶M. D. Renzo, F. Graziosi, and F. Santucci, “Further results on the approximation of log-normal power sum via pearson type iv distribution: a general formula for log-moments computation,” *IEEE Transactions on Communications* **57**, 893–898 (2009).
- ³⁷A. M. Tishin and Y. I. Spichkin, *The magnetocaloric effect and its applications* (IoP Institute of Physics Publishing, 2003).
- ³⁸M. Foldeaki, W. Schnelle, E. Gmelin, P. Benard, B. Koszegi, A. Giguere, R. Chahine, and T. K. Bose, “Comparison of magnetocaloric properties from magnetic and thermal measurements,” *Journal of Applied Physics* **82**, 309–316 (1997).
- ³⁹O. Peksoy and A. Rowe, “Demagnetizing effects in active magnetic regenerators,” *J. Magn. Magn. Mater.* **288**, 424–432 (2005).
- ⁴⁰A. Smith, K. K. Nielsen, D. V. Christensen, C. R. H. Bahl, R. Bjørk, and J. Hattel, “The demagnetizing field of a nonuniform rectangular prism,” *J. Appl. Phys.* **107**, 103910(1–8) (2010).
- ⁴¹C. R. H. Bahl and K. K. Nielsen, “The effect of demagnetization on the magnetocaloric properties of gadolinium,” *J. Appl. Phys.* **105**, 013916(1–5) (2009).
- ⁴²T. Zhou, L. Peng, Y. Liu, Y. Zhan, F. Liu, and A. Zhang, “An insight into the sequential order in 2d correlation spectroscopy using polymer transitions: Boltzmann sigmoid, gaussian cumulative, lorentz cumulative, and asymmetric sigmoid. findings in experiments and simulations,” *Vibrational Spectroscopy* **70**, 137–161 (2014).
- ⁴³B. P. Vieira, H. N. Bez, M. Kuepferling, M. A. Rosa, D. Schafer, C. C. Plá Cid, H. A. Vieyra, V. Basso, J. A. Lozano, and J. R. Barbosa Jr., “Magnetocaloric properties of spheroidal $\text{La}(\text{Fe,Mn,Si})_{13}\text{Hy}$ granules and their performance in epoxy-bonded active magnetic regenerators,” *Applied Thermal Engineering* **183**, 116185 (2021).
- ⁴⁴T. V. Christiaanse, O. Campbell, P. V. Trevizoli, S. Misra, D. van Asten, L. Zhang, P. Govindappa, I. Niknia, R. Teyber, and A. Rowe, “A concise approach for building the s-T diagram for Mn-Fe-P-Si hysteretic magnetocaloric material,” *J. Phys. D: Appl. Phys.* (2017), accepted for publication.
- ⁴⁵P. V. Trevizoli, A. T. Nakashima, and J. R. Barbosa Jr., “Performance evaluation of an active magnetic regenerator for cooling applications - Part II: Mathematical modeling and thermal losses,” *Int. J. Refrig.* **72**, 206–217 (2016).